Bioactive Materials 14 (2022) 97–109

Contents lists available at ScienceDirect

Bioactive Materials

journal homepage: www.keaipublishing.com/en/journals/bioactive-materials

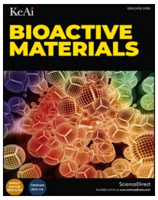

Large-sized bone defect repair by combining a decalcified bone matrix framework and bone regeneration units based on photo-crosslinkable osteogenic microgels

Junxiang Hao[a,c,1], Baoshuai Bai[a,c,1], Zheng Ci[a,c,1], Jincheng Tang[a,c], Guanhuai Hu[d], Chengxiang Dai[e], Mengyuan Yu[d], Meng Li[e], Wei Zhang[a,b,c], Yixin Zhang[b], Wenjie Ren[d,**], Yujie Hua[b,c,***], Guangdong Zhou[a,b,c,*]

[a] *Research Institute of Plastic Surgery, Weifang Medical University, Weifang, Shandong, China*
[b] *Department of Plastic and Reconstructive Surgery, Shanghai 9th People's Hospital, Shanghai Jiao Tong University School of Medicine, Shanghai Key Laboratory of Tissue Engineering, Shanghai, China*
[c] *National Tissue Engineering Center of China, Shanghai, China*
[d] *Institute of Regenerative Medicine and Orthopedics, Institutes of Health Central Plain, Xinxiang Medical University, Xinxiang, Henan, China*
[e] *Cellular Biomedicine Group, Inc., Shanghai, China*

ARTICLE INFO

Keywords:
Microgels
Large-sized bone defect repair
Bone regeneration units
Photo-crosslinking
Decalcified bone matrix)

ABSTRACT

Physiological repair of large-sized bone defects is great challenging in clinic due to a lack of ideal grafts suitable for bone regeneration. Decalcified bone matrix (**DBM**) is considered as an ideal bone regeneration scaffold, but low cell seeding efficiency and a poor osteoinductive microenvironment greatly restrict its application in large-sized bone regeneration. To address these problems, we proposed a novel strategy of bone regeneration units (**BRUs**) based on microgels produced by photo-crosslinkable and microfluidic techniques, containing both the osteogenic ingredient **DBM** and vascular endothelial growth factor (**VEGF**) for accurate biomimic of an osteoinductive microenvironment. The physicochemical properties of microgels could be precisely controlled and the microgels effectively promoted adhesion, proliferation, and osteogenic differentiation of bone marrow mesenchymal stem cells (BMSCs) *in vitro*. **BRUs** were successfully constructed by seeding BMSCs onto microgels, which achieved reliable bone regeneration *in vivo*. Finally, by integrating the advantages of **BRUs** in bone regeneration and the advantages of **DBM** scaffolds in 3D morphology and mechanical strength, a **BRU**-loaded **DBM** framework successfully regenerated bone tissue with the desired 3D morphology and effectively repaired a large-sized bone defect of rabbit tibia. The current study developed an ideal bone biomimetic microcarrier and provided a novel strategy for bone regeneration and large-sized bone defect repair.

1. Introduction

Bone injury is a common disease that remains a serious problem as the associated loss of function considerably impairs the quality of patients' life [1–3]. In particular, large-sized bone defects caused by traumatic injury, degenerative disease, or surgical removal of bone tumors have limited regenerative capacity; thus, the repair of large-sized bone defects is a major challenge [4–7]. Currently, bone tissue engineering has emerged as an attractive technique for bone regeneration through culturing osteogenic cells on biocompatible scaffolds [8–11]. However, there have been no significant clinical breakthroughs in repair of large-sized bone defects due to the lack of ideal biomimetic scaffolds suitable for osteogenic cell seeding with an appropriate osteoinductive microenvironment. Decalcified bone matrix (**DBM**) has been considered

---

Peer review under responsibility of KeAi Communications Co., Ltd.

[*] Corresponding author. Research Institute of Plastic Surgery, Weifang Medical University, Weifang, Shandong, China.

[**] Corresponding author.

[***] Corresponding author. Department of Plastic and Reconstructive Surgery, Shanghai 9th People's Hospital, Shanghai Jiao Tong University School of Medicine, Shanghai Key Laboratory of Tissue Engineering, Shanghai, China.

E-mail addresses: wjren1966@163.com (W. Ren), hyj137@shsmu.edu.cn (Y. Hua), guangdongzhou@126.com (G. Zhou).

[1] These authors contributed equally: Junxiang Hao, Baoshuai Bai, Ci Zheng.

https://doi.org/10.1016/j.bioactmat.2021.12.013
Received 15 October 2021; Received in revised form 6 December 2021; Accepted 9 December 2021

an ideal bone regeneration scaffold owing to the connatural bone structure, mineralized components, good biocompatibility, and osteogenic activity [12–14]. In fact, **DBM** scaffolds have been widely used for small-sized bone defect repair through activating endogenous bone regeneration. Nevertheless, **DBM** scaffolds are not suitable for repairing large-sized bone defects because of the poor cell seeding efficiency attributed to relatively large and irregular pore structure, and severe loss of osteoinductive components caused by decellularization and decalcification treatments. Additionally, most of the previous studies mainly focus on *in situ* bone defect repair that possess relatively ideal osteogenic microenvironment for bone regeneration [15,16]. The ectopic ossification in the subcutaneous microenvironment has limited applications based on such **DBM** scaffolds, due to the lack of osteoinductive factors for bone regeneration in the ectopic environment, which were much harsher than that of *in situ* bone defects.

Recently, to enhance cell seeding efficiency on scaffolds of large pore size, cell seeding units with certain volume have proven to be a promising strategy. In previous work, microtissues [17,18] (such as cell pellets and cell sheets) or cell-loaded microcarriers [19–23] (such as dextran matrix, hydroxyapatite particles, **DBM** powders, and polymer microparticles) were used for seeding on 3D-printed polymer scaffolds to improve cell seeding efficiency. However, these strategies have difficulties in precisely controlling physicochemical properties of cell seeding units or accurately biomimicking an osteogenic microenvironment. By contrast, photo-crosslinkable microgels [24–29] produced by microfluidics [30–34] have unique advantages for precise controllability in size, uniformity, bioactive substance release, mechanical strength, and degradation rate of microcarriers. More importantly, by means of photo-crosslinkable microgels, the biomimetic osteogenic microenvironment is relatively easily created by optionally adding bioactive substances into microgels to better regulate the osteogenesis and angiogenesis of engineered bone, such as bone morphogenetic proteins (**BMPs**) and vascular endothelial growth factor (**VEGF**) [35–38]. These advantages of photo-crosslinkable microgels are very beneficial for solving the key problems of **DBM** scaffolds in both low seeding efficiency of cells and severe damage to the osteoinductive microenvironment. To date, there have been no reports using photo-crosslinkable microgels with a biomimetic osteogenic microenvironment as cell seeding units on **DBM** scaffolds for large-sized bone defect repair. To investigate the feasibility of the above strategy, the following problems need to be solved: 1) how to controllably prepare photo-crosslinkable microgels with a biomimetic osteogenic microenvironment that is suitable for cell loading; 2) whether osteogenic microgels could facilitate adhesion, proliferation, and osteoinductive differentiation of bone marrow mesenchymal stem cells (BMSCs); 3) whether the combination of cell-laden microgels and a **DBM** scaffold could regenerate engineered bone with the desired 3D morphology; and 4) whether large-sized bone defects could be *in situ* repaired with regenerated bone based on a **DBM** scaffold seeded with cell-laden microgels.

To address the above issues, we developed novel photo-crosslinkable microgels based on a microfluidic technique, which contained osteogenic **DBM** powders and the angiogenic growth factor **VEGF** (see Scheme 1). The physicochemical properties of microgels were precisely controlled in size, uniformity, bioactive substance release, mechanical strength, and degradation rate. Then, bone regeneration units (**BRUs**) were constructed by seeding BMSCs onto photo-crosslinkable microgels, followed by *in vitro* culture. Furthermore, the adhesion, proliferation, and osteogenic differentiation of BMSCs on microgels, as well as the feasibility of bone regeneration based on BMSC-laden microgels were investigated *in vitro* and *in vivo* respectively. Finally, the feasibility of bone regeneration with the desired 3D morphology as well as its application for large-sized bone defect repair in a rabbit tibia model was investigated by combining **BRUs** with a **DBM** scaffold.

2. Experimental section

2.1. Materials and animals

All materials were purchased from Sigma-Aldrich. Both nude mice and New Zealand white rabbits were purchased from Shanghai Jiagan Experimental Animal Raising Farm (Shanghai, China). All protocols for experiments in animals were approved by the Animal Care and Experimental Committee of Shanghai Jiao Tong University School of Medicine (Shanghai, China).

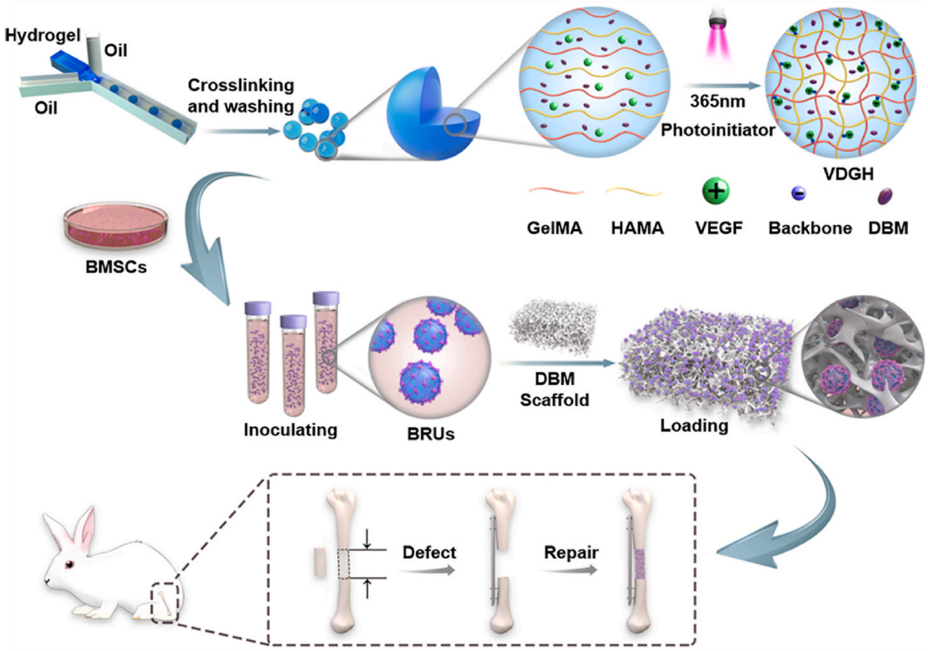

Scheme 1. Schematic illustration of large-sized bone defect repair by combining a decalcified bone matrix framework and bone regeneration units based on photo-crosslinkable osteogenic microgels. **DVGH**: **VEGF**/**DBM**-loaded **GelMA**/**HAMA**; **BRUs**: bone regeneration units.

2.2. Preparation of DBM scaffolds

Fresh pig bone were purchased from a local slaughterhouse, and removed the attached soft tissue, central bone marrow and cartilage. These bone tissue were cleaned with distilled water, and defatted in 30% hydrogen peroxide at 37 °C for 48 h, followed by changing the solution every 24 h. Then, they were soaked in distilled water, and 0.6 M hydrochloric acid was added to partially decalcify at 4 °C for 72 h, followed by changing the solution every 24 h. After the decalcified process, the above samples were soaked in ethanol for 4 h to remove residual hydrogen peroxide, and partially deproteinized at room temperature for 4 h, and cleaned with distilled water. After freeze-drying at −50 °C, 10 Pa for 24 h, the residual antigenicity of collagen was disinfected and removed by 25 KGy radiation, and eventually a partially decalcified bone scaffold was obtained.

2.3. GelMA synthesis

A total of 10 g of gelatin was dissolved in 500 ml PBS (pH = 7.4) and stirred vigorously at a constant speed at 50 °C using a magnetic stirrer. Methacrylate anhydride (10 ml) was slowly added and allowed to react with gelatin for 4 h. After the solution was collected, the portion that did not react was removed using 5,500 rpm centrifugation, and the solution was dialyzed at 40 °C for 1 week using a cut-off membrane (7,000 Da). The above solution was frozen and placed in a lyophilizer to freeze dry for 24 h to obtain a white product. ^{1}H NMR analysis was performed to determine the degree of methacrylation as previously described [39].

2.4. HAMA synthesis

A total of 10 g of hyaluronic acid (340 kDa) was dissolved in 200 ml of deionized water. A magnetic stirrer was used for constant stirring at room temperature for 3 h and then the solution was put into an ice bath. During the process, 40 mL methacrylate anhydride was slowly added at a constant rate. Then, 40 mL of 5 M NaOH solution was slowly added, and the solution was stirred overnight. After the reaction, the solution was collected and the unreacted precipitate was removed using 5,500 rpm centrifugation. A cut-off membrane (7,000 Da) was used to dialyze the solution at 40 °C for 3 days. The above solution was frozen and placed in a lyophilizer to freeze dry for 24 h to obtain white product. ^{1}H NMR analysis was performed to determine the degree of methacrylation as previously described [40].

2.5. Microgels production

To produce VDGH microgels, 500 mg GelMA and 100 mg HAMA were dissolved in 10 ml PBS solution containing 0.2 μg/ml VEGF, 10 mg/ml DBM powders (Daqing Biotechnology Co., LTD), and 4 mg/ml lithium phenyl-2,4,6-trimethylbenzoylphosphinate (LAP) photoinitiator. The above solution was dissolved at 40 °C for 30 min as the dispersed phase (water phase). A total of 5 ml SP 80 was added to 40 ml paraffin oil and preheated at 40 °C for 10 min as a continuous phase (oil phase). Fluids were injected into the microchannels by micro-pumps, and the dispersed phase formed single spherical droplets under the shear action of the oil phase. A 50 ml centrifuge tube was used to collect the spherical droplets. The collected droplets were polymerized into stable microspheres after exposure to UV light (365 nm, 20 mW/cm^2) for 30 s. The surfactant on the surface of microspheres was washed with hexane and the organic solvent was washed with distilled water. Microspheres with different diameters can be produced by adjusting the flow rates of the water phase and oil phase. We prepared 100 μm, 300 μm, 500 μm and 700 μm microspheres to optimize the particle size of microspheres for cell attachment. The component analysis of XPS (ESCALAB MK-II), EDS (QUAN-TAX200 Bruker), and XRD (Philips X0 Pert Pro) were conducted to confirm the addition of DBM into GelMA/HAMA microgels.

2.6. Physical characterization of microspheres

Dynamic rheology experiments were performed on a HAAKE MARS III photorheometer with parallel-plate (P20 TiL, 20-mm diameter) geometry and OmniCure Series 2000 (365 nm, 20 mW/cm^2). Time sweep oscillatory tests were performed at a 10% strain (CD mode), 1 Hz frequency and a 0.5 mm gap for 180 s. Frequency sweep were oscillatory tests performed to evaluate the storage modulus (G′) and loss modulus (G″) of microgels. AFM-assisted nano-indentation was conducted using a 5 nN force trigger, according to the following parameters: the cantilever spring constant K was 110.56 pnnm^{-1}, and the velocity of the probe was 2 μms^{-1}. The elastic modulus of each microgels was determined using NanoScope Analysis software, which applied the Hertz contact model to the force-displacement curve in the linear region, ranging from 10% to 20% of the strain.

2.7. Degradation tests

For *in vitro* degradation, 1 mg lyophilized sample was added to 1 ml PBS containing 10 U mL^{-1} collagenase and 10 U mL^{-1} hyaluronidase. The initial weight of samples were recoded as W_0 in a dry state. The microgels were incubated for 1 week in 1.5 mL tubes at 37 °C. To ensure a constant enzyme concentration, PBS containing collagenase and hyaluronidase was replaced daily. The liquid in the tubes was removed every 24 h, and samples were washed with deionized water three times. After freeze-drying, the weight of samples were recorded as W_t in a dry state. For *in vivo* degradation, 200 μL of wet VDGH microgels were injected into nude mice through a 1 ml syringe, and the dry weight was recorded as W_0. The samples were harvested at 4W, 8W, and 12W, and the W_t under wet conditions was weighed and recorded. The remaining mass percentages of the samples were calculated at different time points. Each group included three parallel samples.

$$\text{Degradation ratio} = \frac{W_t}{W_0} \times 100\%$$

2.8. Preparation of bone regeneration units

BMSCs were obtained from bone marrow of adult rabbits, and cells from passage two were used in this study. BMSCs were premixed with dry microgels at a concentration of 60 mil/mL, placed in a 50 mL centrifuge tube and incubated at 37 °C for 4 h, so that the cells could fully spread on the surface of microgels. After incubating in a 50 mL centrifuge tube for 48 h, the cell adherent microgels were collected and transferred into petri dishes. Osteogenic differentiation solution (MesenCult™ MSC Basal Medium) was added and cultured in petri dishes for another 12 days. The cell-microgel complex were kept in an incubator at 37 °C with 5% CO$_2$, and the culture medium was changed daily to ensure sufficient nutrient supply to the cells.

2.9. Cell viability

Cell viability was measured at the 1st, 4th, 7th, and 14th days of culture, and the survival rate of BMSCs attached to the surface of microgels was determined. Cell viability was measured and assessed using live/dead staining (calcein-AM/PI) according to the manufacturer's instructions. Live/dead dye solution was prepared by adding 2 μL calcein-AM and 3 μL PI to 1 mL PBS. A total of 10 mg cell-microgel complex was added to 1 mL of live/dead dye solution to stain the cells, which were incubated in the dark at 37 °C for 15 min. After imaging using fluorescence microscopy, NIH Image J software was used to quantitatively analyze the number of living and dead cells, and the cell viability was evaluated by calculating the ratio of the number of living cells to the total number of cells.

2.10. Cell spreading

To observe cell adhesion on the microspheres at days 1, 7, and 14. F-actin and nucleus were separately stained with phyllopeptides and DAPI staining. PBS solution was used to rinse three times repeatedly to remove the remaining medium in the samples, which were then fixed with 4% paraformaldehyde (PFA) for 15 min. After PBS leaching and washing, 5 μg/mL of Gobbi cyclic peptide solution was drop diluted and incubated for 1 h. After washing with PBS, the specimen was incubated in DAPI solution with 1:1,000 dilution for 5 min in darkness, and the nucleus was stained. Tablets were sealed with a sealing solution containing an anti-fluorescence quenching agent. Images were then observed under a fluorescence microscope and the number of cells was measured using NIH Image J software according to the DAPI staining.

2.11. Cell proliferation

The proliferation of BMSCs *in vitro* and *in vivo* was quantitatively determined by DNA ($n = 5$). The cells were digested overnight in 500 μg/mL proteinase K solution at 56 °C. The Picogreen dsDNA method was used to draw a standard curve according to the fluorescence intensity and DNA concentration of the DNA samples, and the DNA concentration of the samples to be tested was obtained according to the standard curve.

2.12. Osteogenic differentiation

To verify the osteogenic differentiation ability of VDGH microgels, cell-laden microgels were cultured in osteogenic induction solution (MesenCult™ MSC Basal Medium) for 2 weeks. The BMSCs collected on day 0 were the same initial state and basically had no significant differences of osteogenic gene expression among all groups. After the 1st, 7th, and 14th days of culture, the expression levels of BMSC genes were determined by fluorescence quantitative PCR ($n = 5$). According to the manufacturer's guidelines, the concentration of the extracted protein was measured by the BCA method. After SDS-PAGE electrophoresis, film transfer, and target antibody reaction, the Alpha software processing system was used to analyze the optical density value of the target band ($n = 5$).

2.13. VEGF release study in vitro

A VEGF ELISA kit was used to determine the amount of VEGF in the washing solution, and the encapsulation rate (%) of VEGF in VDGH microgels was calculated using the equation below. Briefly, the standard curve was first determined using the standard samples with a series of concentration gradient, and then the release of VEGF weight was calculated according to the standard curve. The amount of VEGF actually encapsulated by microgels was recorded as M_t. The total amount of VEGF in the initial batch was recorded as M_o.

$$\text{Encapsulation rate of VEGF } (\%) = \frac{M_t}{M_0} \times 100\%$$

2.14. Bone regeneration

Nude mice 4–6 weeks of age weighing about 13 ± 2 g were used in the study. Four animals were included in each group. The animals were operated on under aseptic conditions after being anesthetized with 10% trichloroacetaldehyde hydrate at a dose of 400 mg kg^{-1}. The collected BRUs were subcutaneously injected into nude mice using a 2 ml syringe at a dose of 200 μL to form a mound shape. Additionally, BRUs were injected into the DBM scaffold to ensure uniform dispersion and no outflow. The BRU-DBM scaffolds were subcutaneously implanted in nude mice, and pure DBM scaffold was used as the control group.

2.15. Repair of segmental bone defects

In strict accordance with the regulations of medical animal experiments, 16 six-month-old New Zealand rabbits with an average body weight of 2.5 ± 0.5 kg were divided into BRU-DBM group, cell-free VDGH-DBM group, DBM group and blank group. Under strict sterile conditions, intravenous anesthesia was performed with tenetamine hydrochloride (10 mg kg^{-1}) and zolazepam hydrochloride (10 mg kg^{-1}). The skin of the rabbit's right posterior supporting leg was prepared, and a 5 cm long longitudinal incision was made at the lateral end of the tibia with an iodophor disinfecting cloth. The tibia was cut off with an electric saw to form a bone defect 15 mm long. After ensuring good alignment, plate fixation was done to remove most of the periosteum tissue in the defect area. The carved DBM scaffold was inserted into the defect area (the volume of the defect area is about 400 mm^3, and the volume of the scaffold is about 500 mm^3) and fit exactly with the broken end of the defect. In the BRU-DBM group, the collected BRUs were injected into the DBM scaffold using a 2 ml injector. Finally, the flap covers were closed and the skin was sutured to close the cortical window.

2.16. X-ray and micro CT examinations

X-ray examination of the operative area was performed immediately after the operation. One month and three months after the operation, the rabbits were anesthetized, and the operative area was examined by X-ray. Three months later, the rabbits were euthanized after an overdose of anesthesia. The tibia was removed for micro CT scan and 3D reconstruction. The index of regenerated bone was calculated as bone volume (BV; mm^3), bone mass ratio (BV/TV), bone surface area (BS; mm^2), and the number of bone trabecula (Tb.N).

2.17. Histological analysis

Samples were decalcified with 10% ethylenediamine tetraacetic acid (EDTA) and immersed in paraformaldehyde. After one month of decalcification, the samples were cut from the center along the longitudinal axis. The samples were dehydrated with a graded ethanol series and embedded in paraffin wax. H&E, Masson, ALP, OCN, CoL1 and CD31 staining were performed.

2.18. Statistical analysis

All data were presented as mean ± standard deviation (s.-d.). Differences between the values were evaluated using one-way analysis of variance (ANOVA) with $p < 0.05$ considered statistically significant.

3. Results

3.1. Microfluidic fabrication of GelMA/HAMA microgels

Photo-crosslinkable gelatin and hyaluronic acid hydrogels were chosen to prepare microgels because the mixed components could mimic extracellular matrix (ECM) composition containing both proteoglycans and glycosaminoglycans [41]. ^{1}H NMR spectra demonstrated an 83% substitution degree of methacrylation for methacrylate-modified gelatin (**GelMA**), and a 78% substitution degree of methacrylation for methacrylate-modified hyaluronic acid (**HAMA**) (Fig. S1). **GelMA/HAMA** droplets were first formed through a water in oil emulsion approach by a droplet microfluidic device (Fig. 1A–B), and then subjected to UV radiation (365 nm, 20 mW/cm^2) for 30 s to reach complete crosslinking according to the rheological analysis of **GelMA/HAMA** hydrogels (Fig. S2). After producing microspheres, the residual oil phase was repeatedly washed, followed by lyophilization into dry powders for preservation (Fig. S3). As shown in Fig. 1C, the diameters of the microgel droplets could be adjusted from ~100 μm to ~700 μm dependent on setting the water phase flow rate (Q_w) from ~5

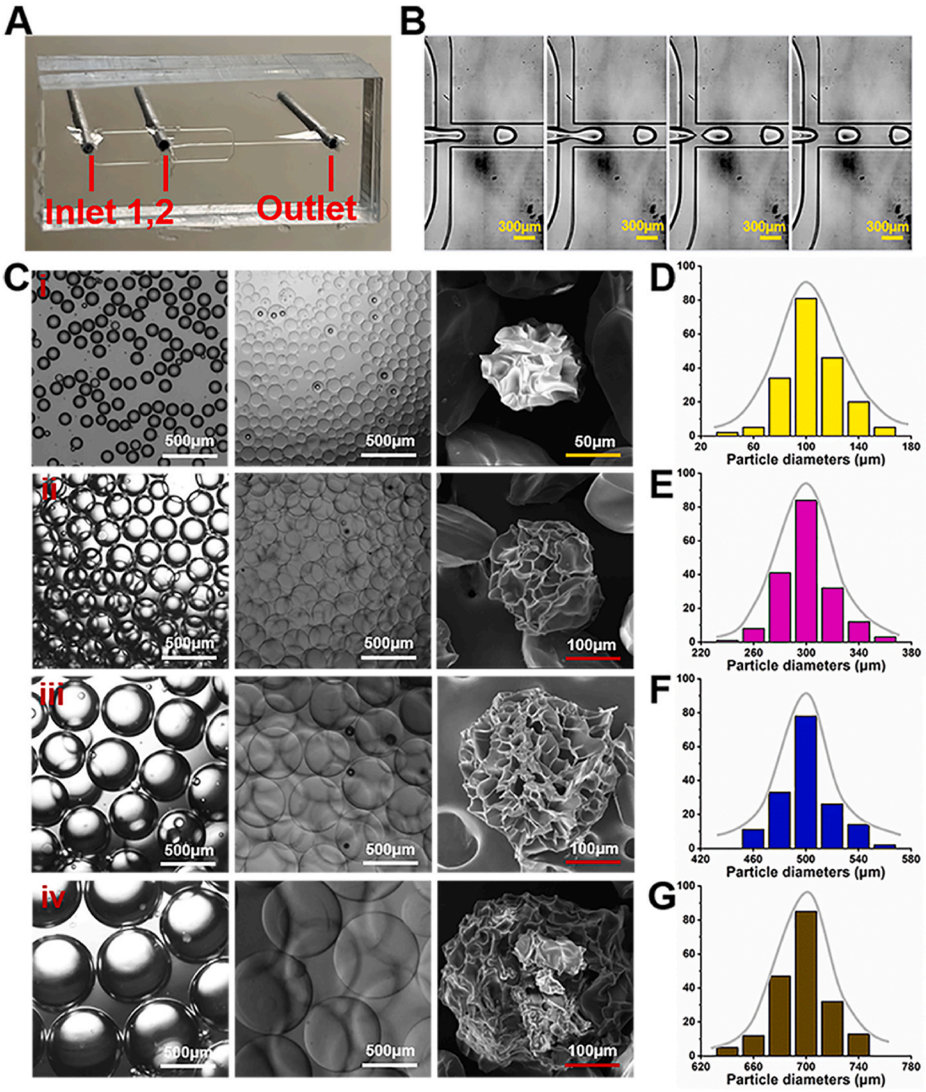

Fig. 1. Microfluidic fabrication of GelMA/HAMA microgels by photo-crosslinking approach. A) Photograph of the microfluidic device. B) Images of **GelMA/HAMA** droplets generated through the microfluidic device. C) Photographs and SEM images of **GelMA/HAMA** microgels of different sizes shown in oil and water phases, *e.g.* 100 μm (i), 300 μm (ii), 500 μm (iii), and 700 μm (iv). D-G) The corresponding particle size distributions of **GelMA/HAMA** microgels.

μL/min to 50 μL/min when the oil phase flow rate (Q_o) was kept constant at 100 μL/min. Scanning electron microscopy (SEM) images showed the wrinkled and porous structure on the surface of lyophilized microspheres, which is beneficial for cell attachment on the microgel surface. In addition, the monodispersity graphs exhibited the well-dispersed distribution of all particle sizes, indicating the satisfactory monodisperse property of microgels produced by the microfluidic method (Fig. 1D–G). The microscopic atomic force microscopy (AFM) results also confirmed that the surface roughness of microgels with different particles sizes had no significant difference, and thus all of which were suitable for cell loading (Fig. S4).

3.2. Optimization and characterization of osteogenic VDGH microgels

To further create an osteogenic microenvironment for **GelMA/HAMA** microgels, **DBM** powders and **VEGF** were chosen as osteogenic and angiogenic biomimics, respectively. SEM images showed that **DBM** powders had micron-scale size (~20 μm) and retained bone-specific **ECM** traits [42] (Figs. 2A and S5). Consistent with the construction of **GelMA/HAMA** microgels, the **VEGF/DBM**-loaded **GelMA/HAMA** (**VDGH)** microgels were also produced with the above droplet microfluidic method using a hybrid water phase (5%w/v **DBM**, 10%w/v **GelMA**, 1%w/v **HAMA**, and 0.2 μg/mL **VEGF**). As shown in Fig. 2B, **VDGH** microgels could be controlled at 300–400 μm in diameter with good monodispersity. Additionally, a uniform distribution of **DBM** powders was clearly observed inside these transparent microspheres, and the lyophilized microgels had a typical porous structure on the surface as shown in SEM images. The constituent analysis of X-ray photoelectron spectroscopy (XPS), energy dispersive X-ray spectroscopy (EDS), and X-ray diffraction (XRD) together revealed the successful addition of **DBM** particles into **GelMA/HAMA** microgels (Fig. S6). The stiffness of microgels evaluated by the macroscopic rheological tests demonstrated that the addition of 1% **HAMA** into 10% **GelMA** resulted in an increase of the elastic modulus, while the 5% **DBM** powders inside the microgels exhibited significantly enhanced mechanical strength (Fig. S7). Moreover, AFM tests also demonstrated that the elastic modulus was strengthened from 2.36 ± 0.84 kPa (**GelMA** microgel) to 14.62 ± 0.79 kPa (**GelMA/HAMA** microgel). Notably, the **DBM**-loaded microgels displayed heterogeneous mechanical behavior in which the region of adjacent **DBM** powders showed a huge elastic modulus of 204.77 ± 24.37 kPa, while other gel regions still exhibited a relatively low elastic modulus of 18.45 ± 1.74 kPa (Fig. 2C). Enzyme-linked immunosorbent assay (ELISA) showed that the encapsulation efficiency of **VEGF** reached approximately 86% in the **GelMA/HAMA**

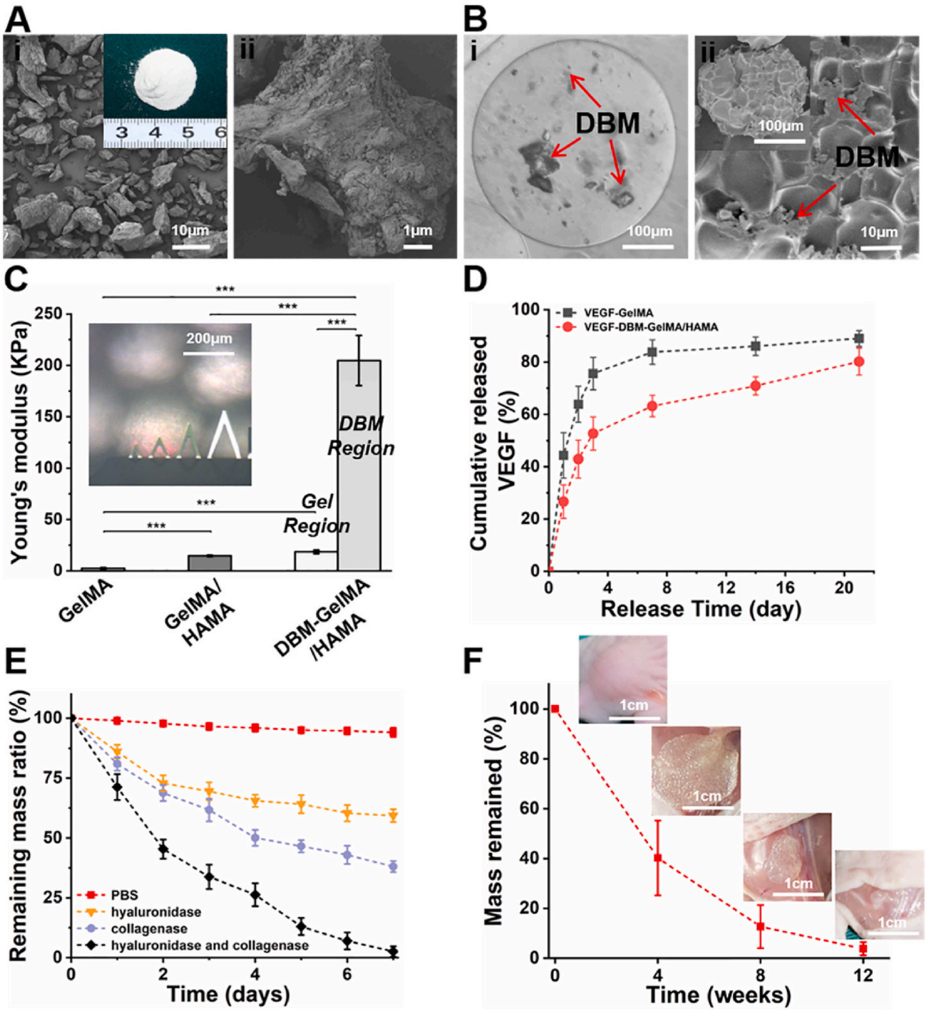

Fig. 2. Characterization of osteogenic VDGH microgels. A) Gross view, low-power (i) and high-power (ii) SEM images of **DBM**. B) Photograph of **VDGH** microgels indicating **DBM** powders dispersed inside the microgels (i). SEM images and surface views of **VDGH** microgels (ii). Red arrows represent **DBM**. C) Young's modulus of the microgels tested by AFM. The Young's moduli of **VDGH** (**DBM** region) were significantly higher than those of other microgels (**GelMA** and **GelMA/HAMA**), and **VDGH** (Gel region). D) The cumulative release of **VEGF** in **VG** and **VDGH** microgels. E) The remaining mass ratio in PBS and different enzyme solutions showing the *in vitro* degradation of **VDGH** microgels. F) *In vivo* degradation evaluation of **VDGH** microgels in the subcutaneous environment of nude mice. **VG**: **VEGF**-loaded **GelMA**; **VDGH**: **VEGF/DBM**-loaded **GelMA/HAMA**. Statistical significance: ***$p < 0.001$. (For interpretation of the references to colour in this figure legend, the reader is referred to the Web version of this article.)

microgels. **VEGF** release exhibited a satisfactory tendency with relatively low burst release (about 27%) at 24 h, acceptable early release (about 53%) at day 3 and continuous, slow release after day 7 (about 63%), likely attributed to the ionic interaction between the negatively charged **GelMA/HAMA** backbone (isoelectric point 5.0) and positively charged **VEGF** (isoelectric point 8.5) at a physiological pH value [43] (Fig. 2D). *In vitro* degradation experiments showed that the **GelMA/-HAMA** microgels were completely degraded in mixed enzyme solution (20 U mL^{-1} hyaluronidase and collagenase in D-PBS) at day 7 but not in individual enzyme solution (Fig. 2E). *In vivo* degradation behavior demonstrated a gradually decreasing tendency with nearly complete degradation after 12 weeks (Fig. 2F). These results indicated that the **VDGH** microgels possessed high mechanical strength, an appropriate biodegradation rate, and controllable **VEGF** release.

3.3. *In vitro biological function evaluation of VDGH microgels*

Biological function of **VDGH** microgels was evaluated by toxicity, adhesion, viability, and proliferation of cells as well as ECM production. As shown in Fig. S8, extraction of **VDGH** microgels did not show obvious cytotoxicity but had a proliferative capacity for BMSCs. Cell adhesion experiments demonstrated that 300 μm microgels using 60 mil/mL cell inoculation density achieved the optimal cell loading efficiency (over 60%; Fig. 3A–B). Cell counts, live/dead, and phalloidin staining demonstrated that BMSCs continuously proliferated from day 1 to day 14 with high cell viability (Fig. 3C–E). Both phalloidin staining and SEM images showed that adherent BMSCs had a spreading morphology with abundant ECM deposition to completely cover the surface of whole microgels at day 14 (Fig. 3D and F). Collectively, these results demonstrated that the microgels had satisfactory biological function in terms of cell adhesion, proliferation, and ECM production.

3.4. *In vitro osteogenic differentiation of BMSCs on VDGH microgels*

To investigate the effect of the **VDGH** microenvironment on the osteogenic differentiation of BMSCs, BMSC-laden **VEGF/DBM-GelMA/HAMA** (**B-VDGH**) microgels were *in vitro* cultured in an osteogenic culture system for 14 days to form bone regeneration units (**BRUs**) as the experimental group, while BMSC-laden **DBM-GelMA/HAMA** (**B-DGH**) and **GelMA/HAMA** (**B-GH**) microgels were the control groups. As shown in Fig. 4A–E, the expression levels of bone-related genes (*ALP*, *BSP*, and *OCN*) and proteins (ALP, BMP-2, OCN, and VEGF) were significantly upregulated in the **BRU** group compared to the other two groups ($p < 0.05$, $n = 4$). The expression levels of bone-related genes (*OCN* and *RUNX2*) and proteins (OCN and VEGF) were also slightly upregulated in the **B-DGH** group compared to the **B-GH** group ($p < 0.05$, $n = 4$). These results demonstrated that both **DBM** and **VEGF** created microenvironments effectively promoted osteogenic differentiation of BMSCs while combining **VEGF** and **DBM** resulted in the optimal osteoinductive microenvironment.

3.5. *In Vivo osteogenic potential of BRUs*

To further evaluate the osteogenic ability of **BRUs**, *in vivo* osteogenic

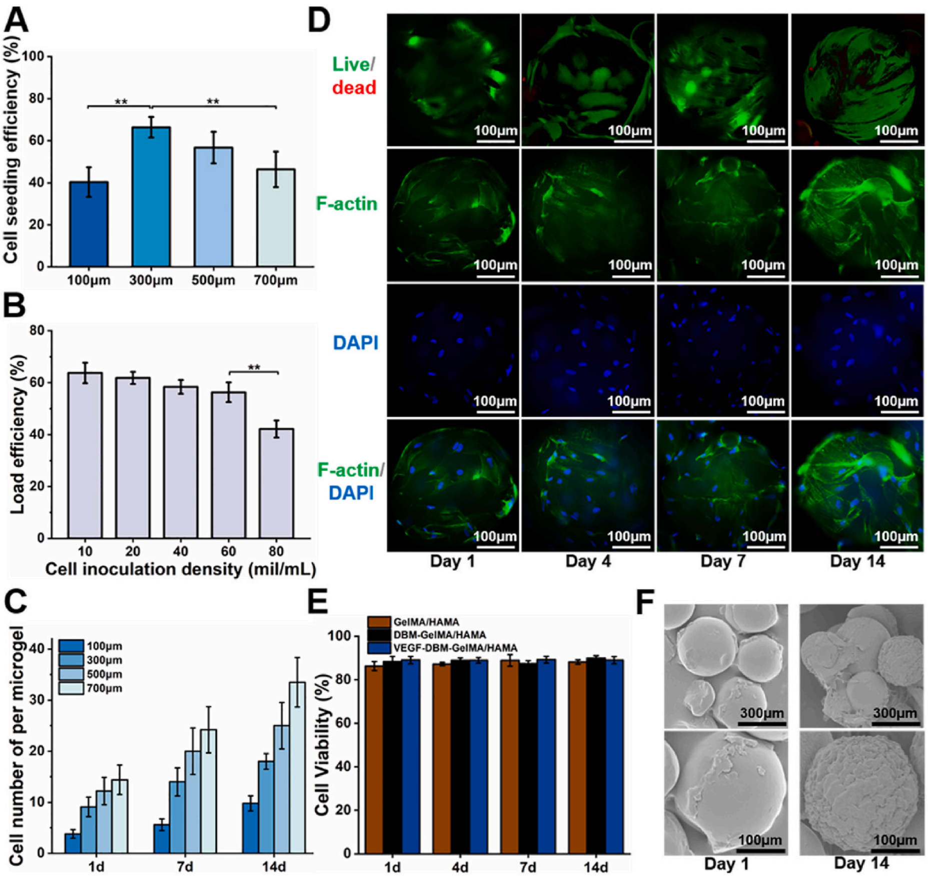

Fig. 3. Biological functional evaluation of cell-laden VDGH microgels *in vitro*. A) Cell seeding efficiencies on **VDGH** microgels of different particle sizes. B) The cell loading efficiency decreased significantly when the cell concentration increased to 80 mil/mL. C) The cell number (per microgel) proliferated on **VDGH** microgels of different particle sizes on days 1, 7, and 14. D) Live/Dead staining showed the live cells (green) increase over time with few dead cells (red). F-actin (green) and DAPI (blue) staining showed the cellular morphology and a gradual increasing trend during *in vitro* culture at days 1, 4, 7, and 14. E) Cell viability on different microgels (**GH**, **DGH**, and **VDGH**) during *in vitro* culture at days 1, 4, 7, and 14. F) SEM images show that the cells and extracellular matrix on the surface of the **VDGH** microgels increased after 14 days of *in vitro* culture. **GH**: **GelMA/HAMA** microgels; **DGH**: **DBM**-loaded **GelMA/HAMA**. Statistical significance: $^{**}p < 0.01$. (For interpretation of the references to colour in this figure legend, the reader is referred to the Web version of this article.)

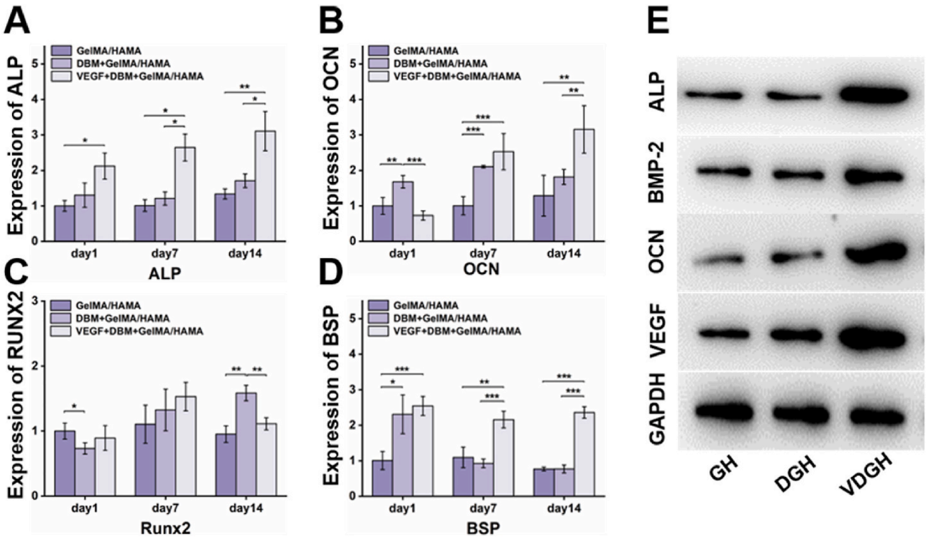

Fig. 4. *In vitro* osteogenic differentiation on VDGH microgels. A-D) *In vitro* osteogenic gene expression (*ALP*, *OCN*, *RUNX2* and *BSP*) of BMSCs after culturing on **VDGH** microgels for days 1, 7, and 14. E) Comparison of osteogenic-related proteins (ALP, BMP-2, OCN, and VEGF) cultured on **GH** microgels, **DGH** microgels, and **VDGH** microgels by Western blot. Statistical significance: $^{*}p < 0.05$, $^{**}p < 0.01$, $^{***}p < 0.001$.

experiments were conducted by subcutaneously injecting **BRUs** into the nude mice (Fig. 5A). The **BRUs** could be easily injected through a 16G syringe head, demonstrating appropriate injectability for minimally invasive delivery (Fig. S9). The implanted samples successfully regenerated bone-like tissue with a reddish appearance and obvious ossification (based on micro-CT) at both 4 and 8 weeks (Fig. 5B), indicating reliable vascularization and new bone formation. Quantitative analysis in Young's modulus, wet weight, volume, volume of new bone (BV), ratio of new bone volume to total volume (BV/TV), bone surface area (BS), and number of trabeculae (Tb.N) revealed a significant increase from 4 weeks to 8 weeks (Figs. 5D–H and S10), implying time-dependent bone regeneration and maturation. The DNA content at 8 weeks decreased slightly compared to 4 weeks (Fig. 5C), which might be related to partial cell apoptosis caused by mineralization during bone

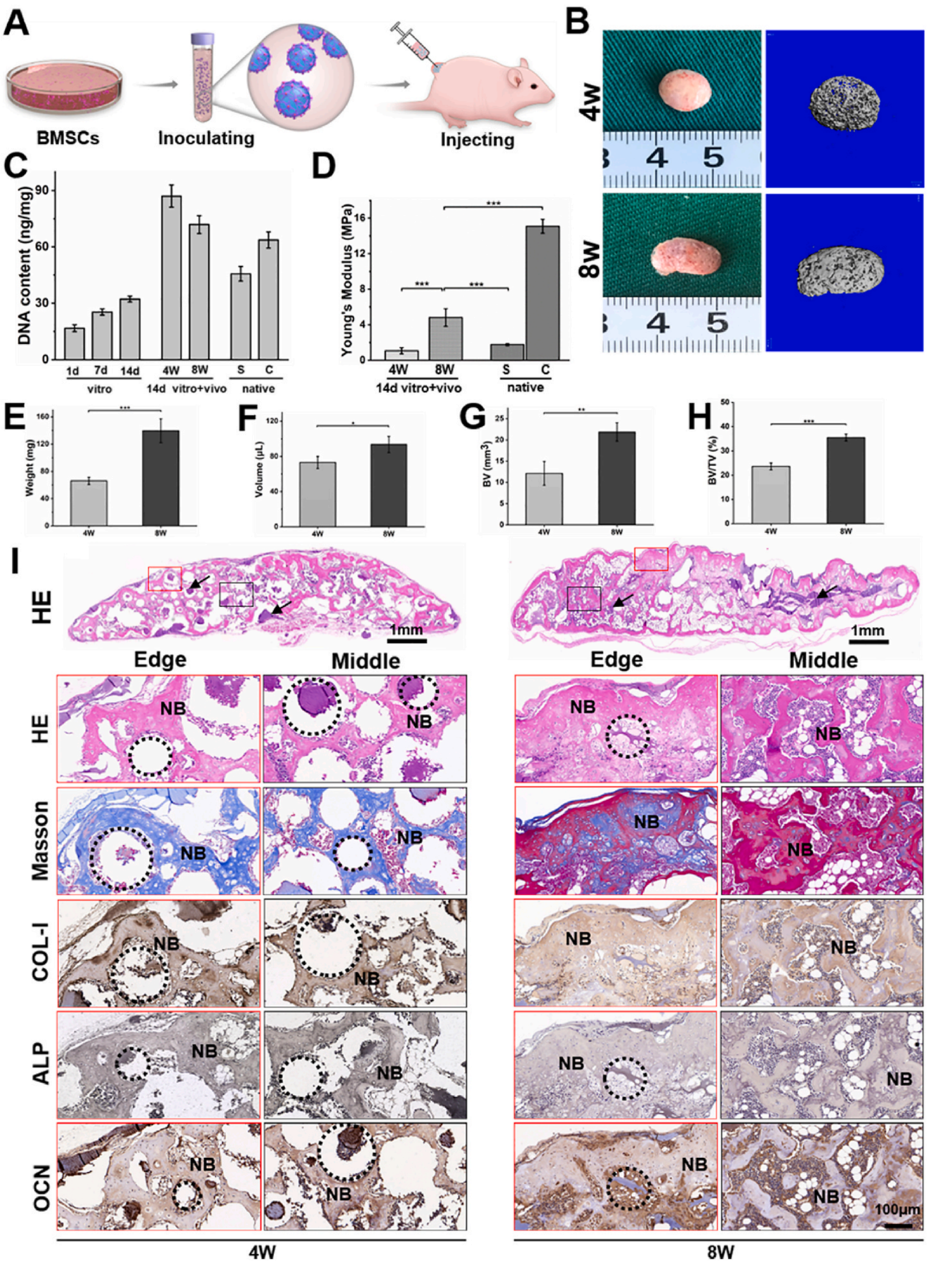

Fig. 5. ***In Vivo* osteogenic potential of BRUs.** A) Schematic of preparation and injection of **BRUs**. B) Gross observation and corresponding micro-CT plain scanning after *in vivo* implantation for 4 and 8 weeks. C–H) Quantitative indexes of DNA content (C), Young's modulus (D), wet weight (E), volume (F), the volume of new bone (BV, G), and bone volume/total volume (BV/TV, H) demonstrate the gradual maturation of regenerated bone tissue. I) Histological analysis of hematoxylin & eosin (H&E) and Masson trichrome (MT) staining show new spongy bone structure, and the new bone was denser at 8 weeks. Immunohistochemistry staining confirmed the specific expression of type I collagen, ALP and OCN. Statistical significance: $^*p < 0.05$, $^{**}p < 0.01$, $^{***}p < 0.001$. **BRUs**: bone regeneration units; **NB**: new bone; **G**: microgels; **S**: spongy bone; **C**: compact bone; black arrows and the dotted circle represent nondegraded microgels.

maturation.

Consistent with gross observation and quantitative analysis, histological examinations further confirmed that the *in vitro* pre-cultured **BRUs** achieved preliminary bone formation with cancellous bone-like structure surrounding the microgels after 4 weeks of subcutaneous injection. The **BRUs** also successfully regenerated relatively mature bone tissue with sufficient bone-specific ECM deposition, typical bone trabecular structure and abundant blood vessels infiltration at 8 weeks (Figs. 5I and S11), indicating that **BRUs** are reliable for bone regeneration.

3.6. *In Vivo bone regeneration of the* ***BRU****-loaded* ***DBM*** *framework*

BRUs were further seeded into the **DBM** framework to explore the feasibility of bone regeneration with the desired 3D morphology. Microscopy and SEM images showed that **DBM** scaffolds presented millimeter-scaled porous structure (Figs. 6A–B and S12), and were exactly suitable for loading of **BRUs** with relatively uniform diameters of about 300 μm (approximately 20–25/mm^3; Figs. S13A and B). Additionally, the loading amount could be adjusted dependent on the microgel size of **BRUs** (such as 100, 300, 500, and 700 μm) in a controllable way (Fig. S13C). After 4 and 8 weeks of subcutaneous implantation *in vivo*, both **DBM** scaffolds (**DBM** group) and **BRU**-loaded **DBM** frameworks (**BRU-DBM** group) basically maintained their original size and shape, but only the **BRU-DBM** group formed bone-like tissue with a reddish appearance and significantly enhanced mechanical strength (Fig. S14). Histological examinations further demonstrated that new bone formation, evidenced by typical structures of bone lacuna and bone trabecula as well as positive expression of bone-related proteins ALP and OCN, was only observed in the **BRU-DBM** group but not in the **DBM** group (Fig. 6C). Furthermore, newly generated bone ECM and bone trabecula derived from **BRUs** tightly integrated with the **DBM** framework to form whole bone tissue. Semi-quantitative analysis of vascularization and new bone formation showed that blood vessel number and new bone area presented an increasing trend from the **B-GH-DBM** group and **B-DGH-DBM** group to the **BRU-DBM** group

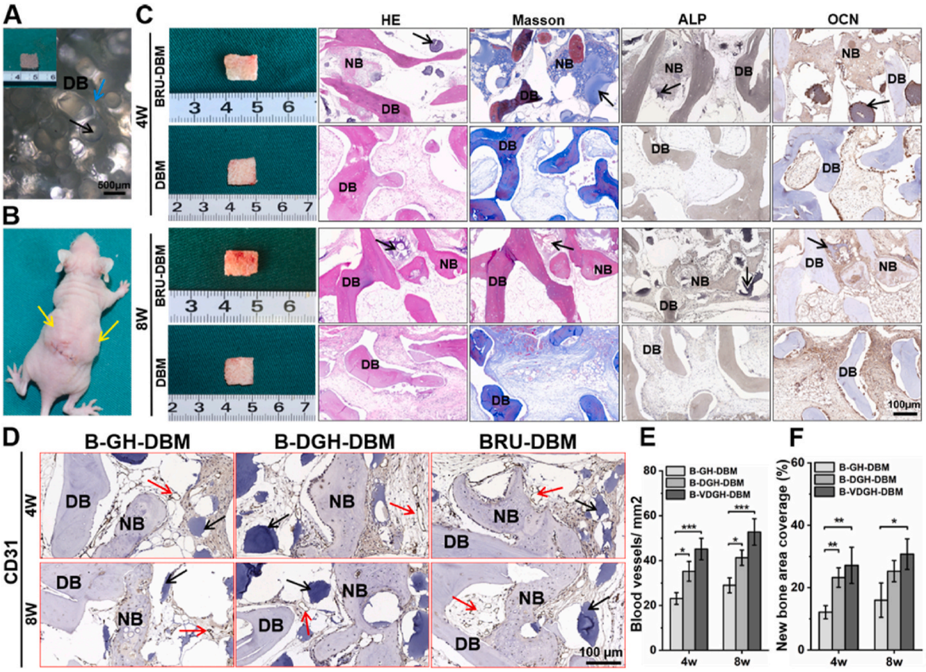

Fig. 6. *In Vivo* bone regeneration of the BRU-loaded DBM framework. A, B) General view and subcutaneous implantation of **BRU**-loaded **DBM** scaffold. C) Gross observation and histological staining of H&E, Masson trichrome, and immunohistochemistry staining of ALP and OCN after 4 and 8 weeks of implantation, showing new bone tissue was evenly distributed in the scaffold. D) Representative immunohistochemistry staining of CD31 after *in vivo* implantation for 4 and 8 weeks showed more blood vessels grew into the **BRU-DBM** scaffold. E, F) Quantitative analysis of blood vessel number (E) and new bone area (F) using ImageJ software. **B-GH-DBM**: BMSCs-laden **GelMA/HAMA** microgels seeding on **DBM** scaffold; **B-DGH-DBM**: BMSCs-laden **DBM-GelMA/HAMA** microgels seeding on **DBM** scaffold; **BRU-DBM**: bone regeneration unit-loaded **DBM** scaffold. **NB**: new bone. **DB**: **DBM** scaffold. Red arrows represent new blood vessels; black arrows represent microgels; blue arrows represent porous structure. (For interpretation of the references to colour in this figure legend, the reader is referred to the Web version of this article.)

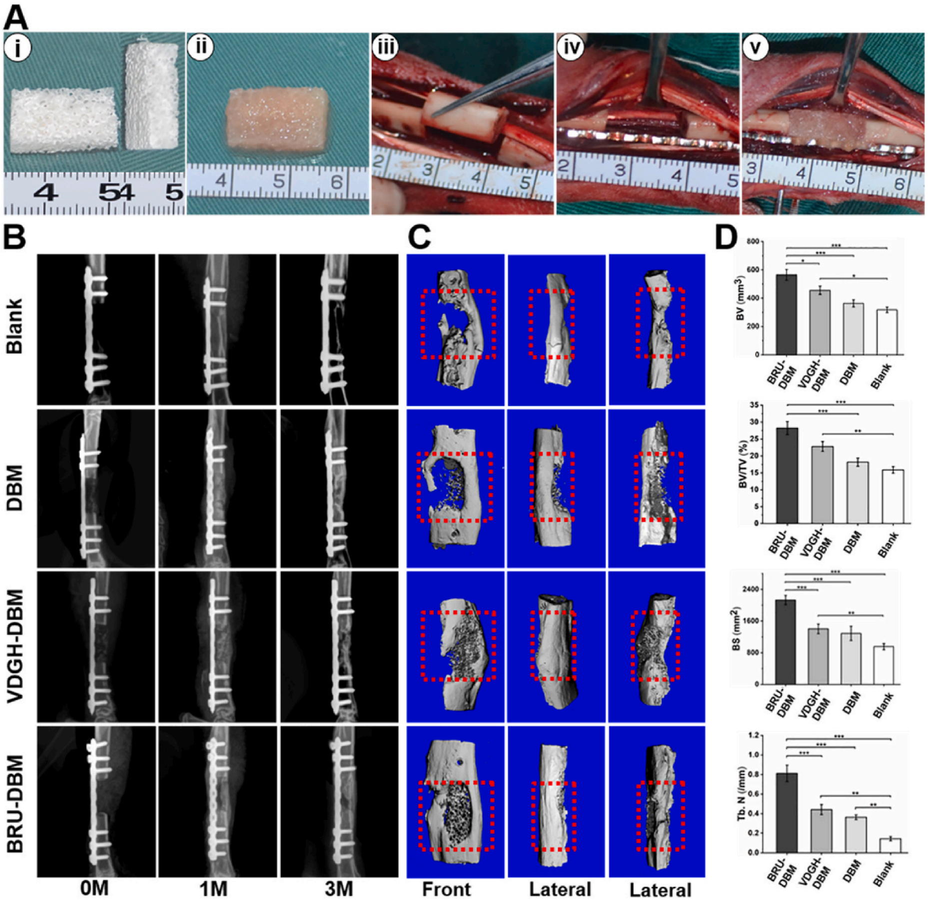

Fig. 7. Repair of large-sized bone defects based on BRU-loaded DBM framework. A) Preparation of **BRU-DBM** scaffold (i-ii), and surgical procedures of implanting **BRU-DBM** scaffold (iii-v). B–C) X-ray (B) and micro-CT (C) examinations of regenerated bone tissue after implantation for 0-month, 1-month, and 3-months. D) Quantitative indexes of bone volume (BV), bone volume/total volume (BV/TV), bone surface (BS), and number of bone trabecula (Tb. N).

(Fig. 6D–F), implying that adding both **DBM** and **VEGF** in microgels promoted vascularization and bone regeneration. These results demonstrated that the combined **BRUs** and **DBM** framework was a reliable strategy for bone regeneration with the desired 3D morphology.

*3.7. Repair of large-sized bone defects based on **BRU**-loaded **DBM** framework*

To further verify the clinical potential of the new strategy, the **BRU**-loaded **DBM** framework (**BRU-DBM** group), **VDGH**-loaded **DBM** framework (**VDGH-DBM** group), and **DBM** framework (**DBM** group) with prefabricated sizes were used to repair large-sized segmental bone defects (15-mm length) in the tibia region of rabbits (Fig. 7A). As shown in Fig. 7B–C, after 3 months, both X-ray and micro-CT examinations demonstrated that the **BRU-DBM** group exhibited abundant new bone formation in the whole bone defect area with relatively complete and continuous bone integration at both edges of the defects, which had recovered to normal function of movement and activities. Obvious bone regeneration with satisfactory bone integration was also observed in the **VDGH-DBM** group but a visible bone regeneration deficiency remained in the central area of the bone defect. Little bone regeneration with obvious bone defects were observed in the **DBM** group and the untreated blank group. Quantitative analysis of BV, BV/TV, BS, and Tb.N further supported optimal bone regeneration in the **BRU-DBM** group (Fig. 7D). Noticeably, most quantitative indexes in the **VDGH-DBM** group were higher than those in the **DBM** group and the untreated blank group, implying that the biomimetic osteoinductive microenvironment created by **VDGH** microgels also played an important role in bone regeneration. The mechanical strength, tested by compression and three-point bending experiments, also demonstrated the optimal bone regeneration in the **BRU-DBM** group, which higher than those of **VDGH-DBM**, **DBM** and the untreated blank groups (Fig. S15). Additionally, the SEM observation and face-scanning EDS analysis showed that the Ca and P distribution of **BRU-DBM** group were superior than those of **VDGH-DBM**, **DBM** and the untreated blank groups, which were close to native bone tissue (Fig. S16).

Consistent with the above examinations, histological staining of cross-sectional samples demonstrated relatively complete and continuous bone formation with mature bone specific ECM (COL1, ALP, and OCN) deposition and satisfactory bone integration in the whole bone defect area of the **BRU-DBM** group (Fig. 8). However, obvious fibrous tissue formation in the central area of the bone defect and noncontinuous bone integration were observed in the **VDGH-DBM** and **DBM** groups, although visible bone regeneration was found in the unilateral area of bone defects in these groups. In the untreated blank group, there was an obvious tissue defect remaining in the central area of the bone defect.

The above results all indicated that the combined **BRUs** and **DBM** framework was a reliable strategy for repair of large-sized bone defects and both implanted cells in **BRUs** and **VDGH** microgels had important roles in bone regeneration and repair.

4. Discussion

Currently, bone tissue engineering using autologous cells loaded scaffolds has been a promising approach to repair large-sized bone defects. Among all types of scaffolds, **DBM** is considered ideal for bone regeneration owing to the connatural bone structure, mineralized components, good biocompatibility, and certain osteogenic activity. However, poor cell seeding efficiency and severe loss of osteoinductive components result in unsatisfactory bone repair, especially for large-sized bone defects. Here, we developed novel photo-crosslinkable microgels based on a microfluidic technique, which contained both osteogenic ingredient **DBM** powders and angiogenic growth factor **VEGF**. The photo-crosslinkable microgels not only accurately mimicked an osteoinductive microenvironment, but also precisely controlled size, uniformity, bioactive substance release, mechanical strength, and degradation rate. Importantly, osteogenic microgels effectively promoted adhesion, proliferation, and osteogenic differentiation of BMSCs. Furthermore, BMSC-loaded microgels were used to successfully construct **BRUs** by *in vitro* culture and achieved satisfactory bone regeneration *in vivo*. Finally, bone regeneration with the desired 3D morphology as well as its application in large-sized bone defect repair of a rabbit tibia model were successfully achieved with a combined **BRUs** and **DBM** scaffold. Thus, the current work developed a novel bone regeneration microcarrier and provides a new strategy for bone regeneration and repair of large-sized bone defects.

The combined **BRUs** and **DBM** scaffold framework was the core design concept of the current study to achieve large-sized bone regeneration. To fabricate **BRUs**, the controllable preparation of photo-crosslinkable microgels with a biomimetic osteogenic microenvironment suitable for cell loading is the first challenge that we faced. To overcome this challenge, we developed a novel technical system that could precisely control the physicochemical properties of microgels by integrating photo-crosslinkable hydrogels and microfluidic technology to achieve an accurately biomimetic osteogenic microenvironment by adding both osteogenic and angiogenic ingredients. The results demonstrated that by adjusting the ratio of water to oil phase flow rate (microfluidic parameter) and the composite ratio of photo-crosslinkable hydrogels (hydrogel parameter), the physicochemical properties of

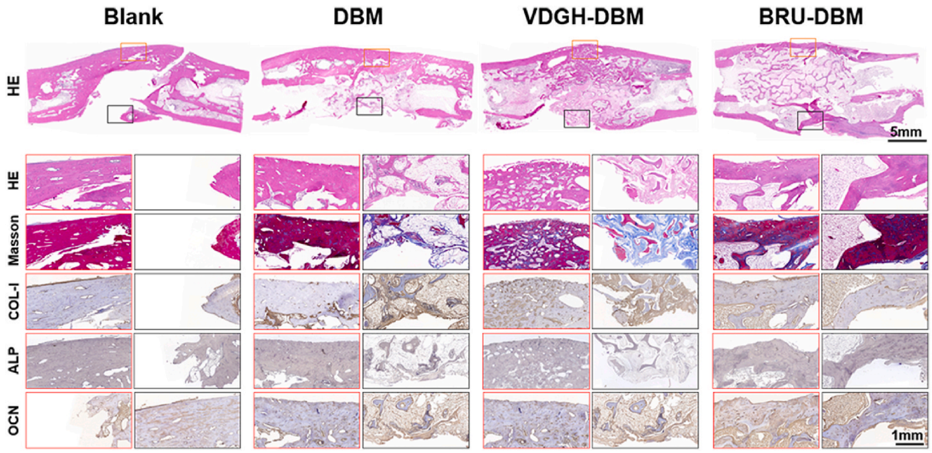

Fig. 8. Histological examinations of specimens obtained from rabbit tibia defects at 3 months post-surgery. The edges of the **BRU-DBM** group formed continuous bone connections compared to the other groups. The **VDGH-DBM** group exhibited more mature bone and effective bone structure than the **DBM** group. In the blank groups, there were large areas of voids and abundant fibroblasts grew into the centers of defects region.

microgels could be precisely controlled in size, uniformity, mechanical strength, and degradation rate. For biomimicking an osteogenic microenvironment, both osteogenic ingredient **DBM** powders and angiogenic growth factor **VEGF** were added into **GelMA/HAMA** hydrogels to prepare photo-crosslinkable microgels (**VDGH**). The results demonstrated that bioactive growth factor could be continuously released from **VDGH** microgels, which was mainly achieved by the ionic interaction between the negatively charged **GelMA/HAMA** backbone and positively charged **VEGF**. In this study, the VEGF-containing **VDGH** microgels not only effectively promote the osteogenic differentiation of BMSCs after 14 days culture *in vitro* (correlated with Fig. 4A–D), but also possess the angiogenic effect on the subcutaneous bone regeneration *in vivo* (correlated with Fig. 6D).

Whether the osteogenic microgels could be used to construct **BRUs** was the next challenge. To avoid cell damage caused by long-term illumination of ultraviolet light and repeated cleaning using toxic organic solvents during the process of cell-encapsulated microgel preparation as described previously [44,45], we adopted two-step methods to construct **BRUs**: lyophilized microgel preparation followed by cell loading on the surface of microgels. Compared to the previous cell-encapsulated microgel preparation, the current strategy had the following advantages: 1) all the cell damage steps could be finished before cell loading and thus effectively improved cell viability; 2) the lyophilized treatment facilitated cell adhesion on the surface of microgels; 3) cells could directly obtain sufficient nutrients from the culture system without being blocked by gels; and 4) the microgels could be prepared in bulk and serve as universal cell loading microcarriers. The current results demonstrated that the osteoinductive microgels with 300 μm diameter showed satisfactory adhesion, survival, proliferation, and osteogenic differentiation of BMSCs, indicating the feasibility of constructing **BRUs** by the two-step methods. More importantly, adding **DBM** powders and **VEGF** (**VDGH** microgels) efficiently upregulated osteogenic differentiation of BMSCs, which was apparently attributed to the biomimetic osteoinductive microenvironment. Additionally, the expression levels of bone-related genes (such as *ALP*, *BSP*, and *OCN*) in the **VDGH** group were significantly upregulated after *in vitro* culture. Noticeably, the simple addition of **DBM** powders (without **VEGF**) in microgels did not have a robust osteoinductive role, which might be attributed to the encapsulation of **DBM** powders in microgels that thus failed to directly contact BMSCs on the microgel surface. Nevertheless, **DBM** powders still might have a unique function in bone regeneration by strengthening the mechanical properties of microgels (Figs. 2C and S2) and promoting osteogenesis *in vivo* by means of osteoinduction, osteoconduction, and angiogenesis during the degradation of microgels (Fig. 2E–F). To further enhance the osteoinductive function, an osteogenic growth factor (such as **BMPs**) can be added into microgels to achieve controllable release similar to VEGF in future studies.

After *in vitro* construction, whether **BRUs** can stably regenerate bone tissue *in vivo* must be determined. According to the results of this study, the *in vitro* pre-cultured **BRUs** showed preliminary bone formation with cancellous bone-like structure surrounding the microgels after 4 weeks of subcutaneous injection, and successfully regenerated relatively mature bone tissue with a mechanical strength higher (2.7-fold) than cancellous bone at 8 weeks, indicating reliable bone regeneration. The stable bone regeneration potential of **BRUs** is likely attributed to the following advantages compared to traditional bulk hydrogel scaffolds: 1) adherent cells on the microgel surface have sufficient opportunity to contact bone induction signals and realize the interaction and communication of cell-cell and cell-ECM contacts, which greatly accelerates osteogenic differentiation of BMSCs; 2) the macroporous structure between these microspheres ensures sufficient nutrient penetration and transport; 3) the space between microgels together with the angiogenic biomimetic microenvironment (continuous release of **VEGF**) are beneficial for blood vessel ingrowth and thus further facilitate vascularization of regenerated bone tissue; and 4) **BRUs** have satisfactory injectability, providing a potential application in minimally invasive injectable bone regeneration. Furthermore, to overcome the 3D morphology deficiency of injectable **BRUs**, a **DBM** scaffold was adopted as a framework to support 3D morphology and mechanical strength of **BRUs**. The current study demonstrated that combining **DBM** scaffolds and **BRUs** successfully regenerated mature bone tissue with the desired 3D morphology, sufficient bone-specific ECM deposition, typical bone trabecula structure, and abundant angiogenesis. Noticeably, the regenerated bone trabecula derived from **BRUs** satisfactorily integrated with the undegraded **DBM** framework and thus formed whole bone tissue with a mechanical strength much higher than **DBM** scaffolds alone (Fig. S9). This novel strategy not only solves the problems of injectable **BRUs** in 3D morphology control and mechanical strength, but also overcomes the deficiencies of **DBM** scaffolds in cell seeding efficiency as well as the osteogenic and angiogenic biomimetic microenvironment.

Finally, whether the combination of **DBM** scaffold and **BRUs** could repair large-sized bone defects was a very important preclinical consideration. The current work demonstrated that cell-free **VDGH**-loaded **DBM** scaffolds exhibited a repair effect in segmental tibia defects (15-mm length), that was, to some extent, better than **DBM** scaffolds and untreated groups (shown certain repair effect referred to previous reports [46–49]). Nevertheless, obvious repair deficiencies were observed in integrity, regenerated bone thickness, and bone structure remodeling, which might be related to the lack of abundant cells during endogenous BMSC homing. In contrast, the implantation of **BRU**-loaded **DBM** scaffolds successfully repaired bone defects with complete and continuous regenerated bone tissue. Furthermore, the regenerated bone tissue resulted in a seamless interfacial integration and connection strength with the surrounding native tissue, indicating that adding **BRUs** significantly improved the repair effect. Obviously, a satisfactory repair effect should be attributed to sufficient cell source and an osteogenic, angiogenic biomimetic microenvironment provided by the implanted **BRUs**, as well as the activation of endogenous bone regeneration mediated by native BMSC homing as shown in the group of cell-free **VDGH**-loaded **DBM** scaffolds.

5. Conclusion

In summary, the current study developed a novel strategy for large-sized bone defect repair with a combined **BRUs** and **DBM** framework. The photo-crosslinkable microgels with an osteogenic and angiogenic biomimetic microenvironment were successfully developed and precisely controlled by means of a photo-crosslinking method and microfluidic technique. Furthermore, the microgels effectively promoted adhesion, proliferation, and osteogenic differentiation of BMSCs *in vitro*. Then, **BRUs** were successfully constructed by seeding BMSCs onto the microgels and achieved reliable *in vivo* bone regeneration. Finally, the combined **BRUs** and **DBM** framework successfully regenerated bone tissue with the desired 3D morphology and effectively repaired large-sized bone defects of rabbit tibia. Although some questions (such as larger bone defect repair in a large animal model, preparation of engineered bone with complicated and precise 3D shape, as well as evaluation of biosafety) and mechanism (such as mechanical induction and signal transduction of intrabony nerves) [50,51] still need to be investigated in future, the current study developed an ideal bone biomimetic microcarrier and provided a novel strategy for bone regeneration and large-sized bone defect repair.

CRediT authorship contribution statement

Junxiang Hao: Data curation, Formal analysis, Investigation, Methodology, Software, Validation, Visualization, Writing – original draft. **Baoshuai Bai:** Data curation, Formal analysis, Investigation, Methodology, Software, Validation. **Zheng Ci:** Data curation, Formal analysis, Investigation, Methodology, Software, Validation. **Jincheng Tang:** Data curation, Formal analysis, Software. **Guanhuai Hu:** Data curation, Formal analysis, Methodology. **Chengxiang Dai:**

Methodology, Validation, Visualization. **Mengyuan Yu:** Data curation, Formal analysis, Methodology. **Meng Li:** Methodology, Validation, Visualization. **Wei Zhang:** Investigation, Project administration, Supervision. **Yixin Zhang:** Funding acquisition, Investigation, Resources. **Wenjie Ren:** Formal analysis, Funding acquisition, Investigation, Project administration, Supervision, Writing – review & editing. **Yujie Hua:** Conceptualization, Data curation, Formal analysis, Investigation, Project administration, Supervision, Visualization, Writing – original draft, Writing – review & editing. **Guangdong Zhou:** Conceptualization, Funding acquisition, Investigation, Project administration, Resources, Supervision, Visualization, Writing – original draft, Writing – review & editing.

Declaration of competing interest

The authors declare no competing interests.

Acknowledgements

This research was financially supported by the National Key Research and Development Program of China (2017YFC1103900), the National Natural Science Foundation of China (81871502, 81701843, and 81671837), the Shanghai Excellent Technical Leader (18XD1421500), the Program of Shanghai Academic/Technology Research Leader (19XD1431100), the Shanghai Collaborative Innovation Program on Regenerative Medicine and Stem Cell Research (2019CXJQ01), and the Clinical Research Plan of SHDC (No. SHDC2020CR2045B). The authors also thank Prof. Linyong Zhu’s group (Shanghai Jiao Tong University) for the help with materials’ characterization.

Appendix A. Supplementary data

Supplementary data to this article can be found online at https://doi.org/10.1016/j.bioactmat.2021.12.013.

References

[1] F. Long, Building strong bones: molecular regulation of the osteoblast lineage, Nat. Rev. Mol. Cell Biol. 13 (2012) 27–38.

[2] R. Dimitriou, E. Jones, D. McGonagle, P.V. Giannoudis, Bone regeneration: current concepts and future directions, BMC Med. 9 (2011) 66.

[3] J. Henkel, M.A. Woodruff, D.R. Epari, R. Steck, V. Glatt, I.C. Dickinson, et al., Bone regeneration based on tissue engineering conceptions – a 21st century perspective, Bone Res 1 (2013) 216–248.

[4] H. Petite, V. Viateau, W. Bensaïd, A. Meunier, C. de Pollak, M. Bourguignon, et al., Tissue-engineered bone regeneration, Nat. Biotechnol. 18 (2000) 959–963.

[5] X. Zhang, J. Fan, C. Lee, S. Kim, C. Chen, T. Aghaloo, et al., Apatite-binding nanoparticulate agonist of hedgehog signaling for bone repair, Adv. Funct. Mater. 30 (2020), 1909218.

[6] T. Nonoyama, S. Wada, R. Kiyama, N. Kitamura, M.T.I. Mredha, et al., Double-Network hydrogels strongly bondable to bones by spontaneous osteogenesis penetration, Adv. Mater. 28 (2016) 6740–6745.

[7] S. Bhumiratana, J.C. Bernhard, D.M. Alfi, K. Yeager, R.E. Eton, J. Bova, et al., Tissue-engineered autologous grafts for facial bone reconstruction, Sci. Transl. Med. 8 (2016), 343ra83.

[8] G.L. Koons, M. Diba, A.G. Mikos, Materials design for bone-tissue engineering, Nat. Rev. Mater. 5 (2020) 584.

[9] Y. Li, Y. Xiao, C. Liu, The horizon of materiobiology: a perspective on material-guided cell behaviors and tissue engineering, Chem. Rev. 117 (2017) 4376–4421.

[10] M.A. Woodruff, C. Lange, J. Reichert, A. Berner, F. Chen, P. Fratzl, et al., Bone tissue engineering: from bench to bedside, Mater. Today 15 (2012) 430–435.

[11] G. Turnbull, J. Clarke, F. Picard, P. Riches, L. Jia, F. Han, et al., 3D bioactive composite scaffolds for bone tissue engineering, Bioact. Mater. 3 (3) (2018) 278–314.

[12] Q. Hu, M. Liu, G. Chen, Z. Xu, Y. Lv, Demineralized bone scaffolds with tunable matrix stiffness for efficient bone integration, ACS Appl. Mater. Interfaces 10 (2018) 27669–27680.

[13] D.J. Holt, D.W. Grainger, Demineralized bone matrix as a vehicle for delivering endogenous and exogenous therapeutics in bone repair, Adv. Drug Deliv. Rev. 64 (2012) 1123–1128.

[14] B. Chen, H. Lin, J. Wang, Y. Zhao, B. Wang, W. Zhao, et al., Homogeneous osteogenesis and bone regeneration by demineralized bone matrix loading with collagen-targeting bone morphogenetic protein-2, Biomaterials 28 (2007) 1027–1035.

[15] E. Quinlan, A. Lopez-Noriega, E. Thompson, H.M. Kelly, S.A. Cryan, F.J. O’Brien, Development of collagen-hydroxyapatite scaffolds incorporating PLGA and alginate microparticles for the controlled delivery of rhBMP-2 for bone tissue engineering, J. Contr. Release 198 (2015) 71–79.

[16] Z. Hu, C. Ma, X. Rong, S. Zou, X. Liu, Immunomodulatory ECM-like microspheres for accelerated bone regeneration in diabetes mellitus, ACS Appl. Mater. Interfaces 10 (3) (2018) 2377–2390.

[17] M. Akiyama, H. Nonomura, S.H. Kamil, R.A. Ignotz, Periosteal cell pellet culture system: a new technique for bone engineering, Cell Transplant. 15 (2006) 521–532.

[18] D. Wu, Z. Wang, J. Wang, Y. Geng, Z. Zhang, Y. Li, et al., Development of a micro-tissue-mediated injectable bone tissue engineering strategy for large segmental bone defect treatment, Stem Cell Res. Ther. 9 (2018) 331.

[19] L. Gao, Z. Huang, S. Yan, K. Zhang, S. Xu, G. Li, et al., Sr-HA-graft-Poly(γ-benzyl-l-glutamate) nanocomposite microcarriers: controllable Sr^{2+} release for accelerating osteogenenisis and bony nonunion repair, Biomacromolecules 18 (2017) 3742.

[20] K. Dashnyam, G.Z. Jin, J.H. Kim, R. Perez, J.H. Jang, H.W. Kim, Promoting angiogenesis with mesoporous microcarriers through a synergistic action of delivered silicon ion and VEGF, Biomaterials 116 (2017) 145.

[21] Y. Du, H. Liu, J. Shuang, J. Wang, J. Ma, S. Zhang, Microsphere-based selective laser sintering for building macroporous bone scaffolds with controlled microstructure and excellent biocompatibility, Colloids Surf. B Biointerfaces 135 (2015) 81.

[22] M. Tian, Z. Yang, K. Kuwahara, M.E. Nimni, C. Wan, B. Han, Delivery of demineralized bone matrix powder using a thermogelling chitosan carrier, Acta Biomater. 8 (2012) 753.

[23] J. Yang, J. Liang, Y. Zhu, M. Hu, L. Deng, W. Cui, et al., Fullerol-hydrogel microfluidic spheres for in situ redox regulation of stem cell fate and refractory bone healing, Bioact. Mater. 6 (12) (2021) 4801–4815.

[24] Y.S. Zhang, A. Khademhosseini, Advances in engineering hydrogels, Science 356 (2017), eaaf3627.

[25] J. Thiele, Y. Ma, S.M.C. Bruekers, S. Ma, W.T.S. Huck, 25th anniversary article: designer hydrogels for cell cultures: a materials selection guide, Adv. Mater. 26 (2014) 125.

[26] T.E. Brown, K.S. Anseth, Spatiotemporal hydrogel biomaterials for regenerative medicine, Chem. Soc. Rev. 46 (2017) 6532–6552.

[27] E.R. Ruskowitz, C.A. DeForest, Photoresponsive biomaterials for targeted drug delivery and 4D cell culture, Nat. Rev. Mater. 3 (2018) 17087–17104.

[28] N. Annabi, Y.N. Zhang, A. Assmann, E.S. Sani, G. Cheng, A.D. Lassaletta, et al., Engineering a highly elastic human protein-based sealant for surgical applications, Sci. Transl. Med. 9 (2017) eaai7466.

[29] J. Zhang, Y. Zheng, J. Lee, J. Hua, S. Li, A. Panchamukhi, et al., A pulsatile release platform based on photo-induced imine-crosslinking hydrogel promotes scarless wound healing, Nat. Commun. 12 (2021) 1670.

[30] A.C. Daly, L. Riley, T. Segura, J.A. Burdick, Hydrogel microparticles for biomedical applications, Nat. Rev. Mater. 5 (2020) 20–43.

[31] A.S. Mao, J. Shin, S. Utech, H. Wang, O. Uzun, W. Li, et al., Deterministic encapsulation of single cells in thin tunable microgels for niche modelling and therapeutic delivery, Nat. Mater. 16 (2017) 236–243.

[32] R. Subbiah, C. Hipfinger, A. Tahayeri, A. Athirasala, S. Horsophonphong, G. Thrivikraman, et al., 3D printing of microgel-loaded modular microcages as instructive scaffolds for tissue engineering, Adv. Mater. 32 (2020), 2001736.

[33] Z. Li, X. Zhang, J. Ouyang, D. Chu, F. Han, L. Shi, et al., Ca(2+)-supplying black phosphorus-based scaffolds fabricated with microfluidic technology for osteogenesis, Bioact. Mater. 6 (11) (2021) 4053–4064.

[34] A.S. Caldwell, B.A. Aguado, K.S. Anseth, Designing microgels for cell culture and controlled assembly of tissue microenvironments, Adv. Funct. Mater. 30 (2020) 1907670.

[35] M.M. Martino, P.S. Briquez, E. Güç, F. Tortelli, W.W. Kilarski, S. Metzger, et al., Growth factors engineered for super-affinity to the extracellular matrix enhance tissue healing, Science 343 (2014) 885–888.

[36] D.H.R. Kempen, L. Lu, A. Heijink, T.E. Hefferan, L.B. Creemers, A. Maran, et al., Effect of local sequential VEGF and BMP-2 delivery on ectopic and orthotopic bone regeneration, Biomaterials 30 (2009) 2816–2825.

[37] T. Miao, K.S. Rao, J.L. Spees, R.A. Oldinski, Osteogenic differentiation of human mesenchymal stem cells through alginate-graft-poly(ethylene glycol) microsphere-mediated intracellular growth factor delivery, J. Contr. Release 192 (2014) 57–66.

[38] J. Street, M. Bao, L. deGuzman, S. Bunting, F.V.P. Jr, N. Ferrara, et al., Vascular endothelial growth factor stimulates bone repair by promoting angiogenesis and bone turnover, Proc. Natl. Acad. Sci. U.S.A. 99 (2002) 9656–9661.

[39] J.W. Nichol, S.T. Koshy, H. Bae, C.M. Hwang, S. Yamanlar, A. Khademhosseini, Cell-laden microengineered gelatin methacrylate hydrogels, Biomaterials 31 (2010) 5536–5544.

[40] S.K. Seidlits, Z.Z. Khaing, R.R. Petersen, J.D. Nickels, J.E. Vanscoy, J.B. Shear, et al., The effects of hyaluronic acid hydrogels with tunable mechanical properties on neural progenitor cell differentiation, Biomaterials 31 (2010) 3930–3940.

[41] Y. Zhao, T. Nakajima, J.J. Yang, T. Kurokawa, J. Liu, J. Lu, et al., Proteoglycans and glycosaminoglycans improve toughness of biocompatible double network hydrogels, Adv. Mater. 26 (2014) 436–442.

[42] D. Sharma, C. Ciani, P.A. Marin, J.D. Levy, S.B. Doty, S.P. Fritton, Alterations in the osteocyte lacunar-canalicular microenvironment due to estrogen deficiency, Bone 51 (3) (2012) 488–497.

[43] X. Zhao, S. Liu, L. Yildirimer, H. Zhao, R. Ding, H. Wang, et al., Injectable stem cell-laden photocrosslinkable microspheres fabricated using microfluidics for rapid generation of osteogenic tissue constructs, Adv. Funct. Mater. 26 (2016) 2809.

[44] A. Kang, J. Park, J. Ju, G.S. Jeong, S. Lee, Cell encapsulation via microtechnologies, Biomaterials 35 (2014) 2651–2663.

[45] R. Zhang, L. Xie, H. Wu, T. Yang, Q. Zhang, Y. Tian, et al., Alginate/laponite hydrogel microspheres co-encapsulating dental pulp stem cells and VEGF for endodontic regeneration, Acta Biomater. 113 (2020) 305–316.

[46] W. Jia, G.Y. Lau, W. Huang, C. Zhang, A.P. Tomsia, Q. Fu, Bioactive glass for large bone repair, Adv. Healthc. Mater. 4 (18) (2015) 2842–2848.

[47] C. Wan, Q. He, G. Li, Allogenic peripheral blood derived mesenchymal stem cells (MSCs) enhance bone regeneration in rabbit ulna critical-sized bone defect model, J. Orthop. Res. 24 (4) (2006) 610–618.

[48] Y. Yu, Y. Wang, W. Zhang, H. Wang, J. Li, L. Pan, et al., Biomimetic periosteum-bone substitute composed of preosteoblast-derived matrix and hydrogel for large segmental bone defect repair, Acta Biomater. 113 (2020) 317–327.

[49] G. Chen, Y. Lv, Matrix elasticity-modified scaffold loaded with SDF-1alpha improves the in situ regeneration of segmental bone defect in rabbit radius, Sci. Rep. 7 (1) (2017) 1672.

[50] J. Li, J. Yan, Q. Wan, M. Shen, Y. Ma, J. Gu, et al., Matrix stiffening by self-mineralizable guided bone regeneration, Acta Biomater. 125 (2021) 112–125.

[51] Q. Wan, W. Qin, Y. Ma, M. Shen, J. Li, Z. Zhang, et al., Crosstalk between bone and nerves within bone, Adv. Sci. 8 (7) (2021), 2003390.